Facile hydrothermal synthesis and optical limiting properties of TiO_2-reduced graphene oxide nanocomposites

Aijian Wang,[1] Wang Yu,[1] Yu Fang,[2] Yinglin Song,[2] Ding Jia,[1] Lingliang Long,[1] Marie P. Cifuentes,[3] Mark G. Humphrey[3] and Chi Zhang*[1,3]

[1] China-Australia Joint Research Center for Functional Molecular Materials, Scientific Research Academy, Jiangsu University, Zhenjiang 212013, P. R. China

[2] School of Physical Science and Technology, Soochow University, Suzhou 215006, P. R. China

[3] Research School of Chemistry, Australian National University, Canberra, ACT 2601, Australia

* Corresponding author. Tel: +86-511-8879-7128. chizhang@ujs.edu.cn (Chi Zhang)

Abstract: TiO_2/reduced graphene oxide (RGO) nanocomposites Gx (RGO Titania nanocomposite, x grams tetrabutyl titanate per 0.03 grams RGO, x = 0.25, 0.50, 1.00) were prepared by a hydrothermal method: graphene oxide was reduced to RGO in a 2:1 water:ethanol mixture in the presence of varying quantities of tetrabutyl titanate, which deposited as TiO_2 on the RGO sheets. The nanocomposites were characterized by a combination of Fourier transform infrared spectroscopy, diffuse reflectance ultraviolet-visible spectroscopy, photoluminescence spectroscopy, Raman spectroscopy, X-ray powder diffraction, X-ray photoelectron spectroscopy and transmission electron microscopy studies. The nanocomposite G0.25 exhibits enhanced nonlinear optical properties compared to its individual components, which is ascribed to a combination of mechanisms. The role of defects and electron/energy transfer in the optical limiting performance of G0.25 was clarified with the help of Raman and photoluminescence spectroscopies. Intensity-dependent switching between reverse saturable absorption and saturable absorption behavior was observed with the G0.50 nanocomposite.

1. Introduction

Graphene, a two-dimensional sp^2-hybridized carbon nanosheet, possesses an atomically thin planar geometry, an unusual band structure and a high carrier mobility, and has spurred immense interest in novel graphene-based materials for a variety of technological applications such as nanocomposites, energy-related materials and optoelectronic devices [1-4]. The majority of work on graphene nanocomposites has been based on reduced graphene oxide (RGO) because of the excellent scalability of its synthesis and fact that defect-free graphene sheets have recently become available. Compared to graphene sheets, RGO nanosheets are pock-marked with defects [5]. In contrast to graphene oxide (GO, an electrically insulating material because of the disrupted sp^2 bonding networks), RGO possesses electrical conductivity and electron/hole transporting properties as the π network is restored, which is favorable for the construction of optoelectronic devices [6]. In particular, significant absorption of incident light and ultrafast carrier dynamics per layer result in RGO being a fast absorber over a wide spectral range [7].

Titanium dioxide (TiO_2), a semiconductor material, has been at the forefront of applied research in the fields of optically active coatings, photo-catalysis and energy conversion due to its specific optical and electronic properties, chemical stability, high optical transparency and large refractive index [8,9]. In comparison with pristine TiO_2, nanoscale composite materials containing TiO_2 are more interesting because of their potential applications in optoelectronic and photovoltaic devices [10-12]. Some investigations have indicated that a doping procedure can inhibit the recombination of electron-hole pairs, as this introduces new energy levels in the bandgap, and thus accelerates the transfer of photogenerated electrons [13]. Although some efforts have been made to synthesize TiO_2-based nanocomposites and to investgate their linear optical properties [14,15], the nonlinear optical (NLO) performance of TiO_2-based nanocomposites remains largely unexploited thus far [16].

The advantages of RGO and the attractive merits of TiO_2 suggest that the combination of the two classes of material may lead to new nanocomposite materials that possess novel properties. Indeed, previous studies of RGO/TiO_2 materials have

highlighted the interesting properties of nanocomposites obtained by a variety of approaches [17-19]. In this study, we report the facile hydrothermal syntheses of TiO_2-decorated RGO nanocomposites with varying composition, characterization of the resultant assemblies by a combination of Fourier transform infrared spectroscopy, diffuse reflectance ultraviolet-visible spectroscopy, photoluminescence spectroscopy, Raman spectroscopy, X-ray powder diffraction, X-ray photoelectron spectroscopy and transmission electron microscopy studies, and a systematic evaluation of the influence of the TiO_2 content on the NLO and optical limiting (OL) behavior of the TiO_2/RGO nanocomposites.

2. Experimental

2.1 Materials

Purified natural graphite was purchased from Qingdao Zhongtian Co. Ltd. Tetrabutyl titanate and ethanol were supplied by Shanghai Sinopharm Chemical Reagent Co. Ltd. All other reagents were purchased from commercial suppliers and were used without further purification, unless otherwise stated. Distilled water was used for all experiments.

2.2 Instruments and measurements

Fourier-transform infrared (FTIR) spectra were carried out with a MB154S-FTIR spectrometer (Bomem, Canada) using spectroscopic grade KBr pellets in the range 4000-400 cm^{-1}; spectra were recorded by accumulating 64 scans at a 4 cm^{-1} spectral resolution at room temperature. Raman spectra were recorded at room temperature on a Renishaw inVia Raman Microscope, exciting at 532 nm with an Ar^+ laser. The laser light was focused onto samples by using a microscope equipped with an a×100 objective. UV-Vis spectra were recorded using a Varian Cary 500 spectrophotometer equipped with a diffuse reflectance accessory at room temperature in the range 200-800 nm. A $BaSO_4$ pellet was used as a reflectance standard. Fluorescence spectra were measured using a Fluoro-Max-P spectrofluorimeter. Transmission electron microscopy (TEM) experiments were performed with a JEM-2100 (JEOL), working at 200 kV. Samples for TEM analysis were obtained by spreading a drop of a dilute dispersion of the as-prepared products on amorphous carbon-coated copper grids,

which were then dried in air before transfer to the TEM sample chamber. X-ray powder diffraction (XRD) experiments were carried out at room temperature on a XD-3 diffractometer (Beijing Purkinje General Instrument Co. Ltd, China) by using Cu Kα radiation (λ = 0.15418 nm). X-ray photoelectron spectroscopy (XPS) characterization was performed on a RBD upgraded PHI-5000C ESCA (PerkinElmer) electron spectrometer with a Mg Kα line at 280 eV.

The Z-scan and OL measurement setup used in our study has been described before [20,21]. Linearly polarized 4 ns pulsed laser radiation at 532 nm was used for excitation. For measurements of the NLO properties, all samples were placed in 2 mm quartz cells, and adjusted to have the same transmittance. To avoid cumulative thermal effects interfering with experiments directed at identifying the major OL mechanism, the laser pulses were delivered at a low frequency of 2 Hz; each pulse of light was therefore ensured to encounter fresh sample.

2.3 Preparation of TiO_2-decorated RGO nanocomposites

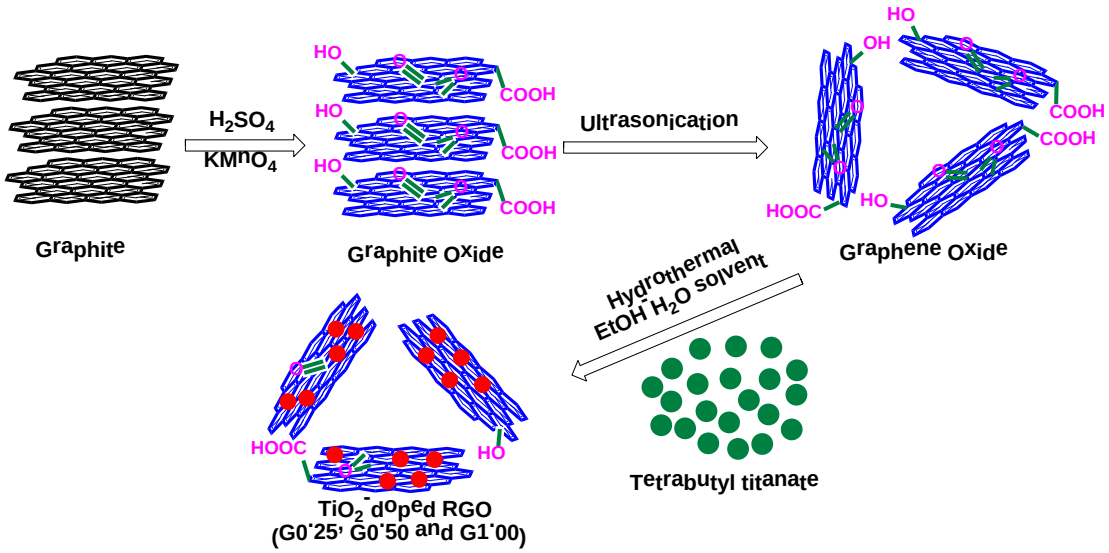

Figure 1. Illustration of the fabrication process for TiO_2-decorated RGO nanocomposites.

GO prepared by a modified method of Hummers and Offeman [22] was used as a substrate for TiO_2 growth, affording TiO_2/RGO nanocomposites. A simple hydrothermal method was used to prepare the nanocomposites, using EtOH-water as

solvent as outlined in Figure 1. Under such solvothermal conditions, EtOH-water can reduce GO to RGO [23,24]. In a typical synthesis, GO (50 mg) was first dissolved in a mixed solution of deionized H_2O (6 mL) and EtOH (3 mL) by ultrasonic treatment for 30 min, resulting in a yellow-brown solution. Tetrabutyl titanate was then added to the GO solution, and the resultant mixture was stirred for a further 30 min to afford a homogeneous suspension. The suspension was placed in a 10 mL Teflon-sealed autoclave that was maintained at 160 ^oC for 72 h. During the hydrothermal process, GO was reduced to RGO with simultaneous deposition of TiO_2 onto the RGO sheet. The resultant composite was collected by centrifugation, washed with distilled water several times followed by a rinsing in EtOH, and then dried under vacuum at room temperature for 18 h. To investigate the effect of TiO_2 content on the NLO properties of the RGO/TiO_2 composites, the weight of tetrabutyl titanate added (as the precursor to TiO_2) was varied (0.25, 0.50, or 1.00 g), the resulting samples being denoted G*x*, where x = 0.25, 0.50 and 1.00, respectively. For comparison, blank RGO and pure TiO_2 were prepared via a hydrothermal route under the same conditions, but without the addition of tetrabutyl titanate or GO, respectively.

3. Results and discussion

3.1 Synthesis

Given the interest in the chemistry of RGO nanocomposites, it is desirable to have convenient dispersion methods to increase the processability and availability of RGO. In this study, a series of RGO/TiO_2 nanocomposites (denoted as G*x*, where *x* represents the amount of tetrabutyl titanate in grams, per 0.03 g of RGO) were prepared by a simple hydrothermal treatment of tetrabutyl titanate and GO in mixed EtOH-H_2O. Under the solvothermal conditions, this results in the facile reduction of GO to RGO, while the nanoparticles of TiO_2 are simultaneously dispersed on the RGO sheets. The fabrication process for the TiO_2-decorated RGO nanocomposites is shown in Figure 1. Stacked graphite is first oxidized to graphite oxide by $KMnO_4$ and 98% H_2SO_4, the graphite oxide containing some oxygen-containing functional groups, such as carboxyl, epoxide and hydroxide. The functional groups on the GO provide reactive anchoring sites for nucleation and growth of nanoparticles. A stable GO

suspension was then obtained by dispersing the graphite oxide in distilled water and EtOH with ultrasonication. The mixed solvent is crucial in controlling the rate of hydrolysis of tetrabutyl titanate. TiO_2/RGO nanocomposites, with different weight addition ratios of tetrabutyl titanate, were then obtained via a hydrothermal method based on a modification of Zhang's procedure [24]. During this process, the hydrothermal temperature was fixed at 160 ^oC, facilitating crystallization of the coating materials on RGO in the anatase phase, and consistent with the approach of Liang et al. [25]. This synthetic strategy for preparing TiO_2-RGO nanocomposites provides several advantages [26,27]: (1) the process is facile, efficient, safe and "green" since it does not use hazardous materials; (2) the closed system at relatively high temperature and internal pressure promotes the recovery of π-conjugation; (3) RGO nanosheets agglomerate and precipitate because of π-π interactions between the sp^2 carbons of RGO sheets after reduction. The problems associated with aggregation of RGO nanosheets in solvents are addressed by introducing direct interactions between the sp^2 carbons of the RGO nanosheets and the TiO_2 precursors; (4) the TiO_2-stabilized RGO solutions display good solution processability, which is favorable for the measurement of photophysical properties; (5) the electron/energy transport properties of RGO nanosheets are improved because of the charge trap screening and doping effects of TiO_2.

3.2 FTIR spectra analysis

Confirmation of TiO_2 functionalization of the RGO sheets was obtained by FTIR spectroscopy. Figure 2 displays typical FTIR spectra of TiO_2, GO, RGO and the nanocomposite materials G0.25, G0.50, and G1.00. In the FTIR spectrum of GO, the most characteristic features are the absorption bands at 3367, 1726, 1363, and 1069 cm^{-1}, corresponding to the O-H groups linked to the basal plane of GO, the C=O stretching vibration of the carboxylic groups, the C-OH stretching vibration, and the C-O stretching vibration, respectively [28]. All of these bands, which are associated with the oxygen-containing functional groups, decrease dramatically in intensity or even disappear after solvothermal reduction, consistent with conversion of GO into RGO. However, a small fraction of the oxygen-containing functional groups persists

and facilitates the hybridizing of the TiO_2 nanoparticles on the RGO sheets. Pure TiO_2 displays a broad IR band between 400 and 1000 cm^{-1}, corresponding to the vibration of the Ti-O-Ti bonds (Figure 2) [29]. An IR band is observed below 1000 cm^{-1} for the TiO_2/RGO nanocomposites; compared to the corresponding band in TiO_2, it is both broader and shifted to higher wavenumber. This band is presumably a combination of Ti-O-Ti vibration and Ti-O-C vibration modes resulting from the chemical interaction of TiO_2 with RGO [30-32]. Deconvolution of the FTIR spectral traces for G0.25, G0.50 and G1.00 in the range from 1080 to 400 cm^{-1} has been effected (inset of Figure 2), confirming the presence of these Ti-O stretching vibrations. The presence of Ti-O-C bands suggests that, during the hydrothermal treatment, the oxygen-containing functional groups of GO interact strongly with the surface hydroxyl groups of the TiO_2 nanoparticles to ensure that the nanoparticles remain attached, even after chemical cleaning and ultrasonication, to eventually afford the chemically-bonded TiO_2/RGO nanocomposites [33]. An absorption band at 1630 cm^{-1} is due to the skeletal vibration of the graphene sheets [23,24]; this peak is also observed in the FTIR spectrum of RGO prepared by hydrothermal reduction of GO. These IR results are consistent with the reduction of GO to RGO, and with grafting of the TiO_2 nanoparticles onto the RGO plane, but do not provide information about different physicochemical properties of the TiO_2/RGO nanocomposites resulting from different addition ratios of TiO_2.

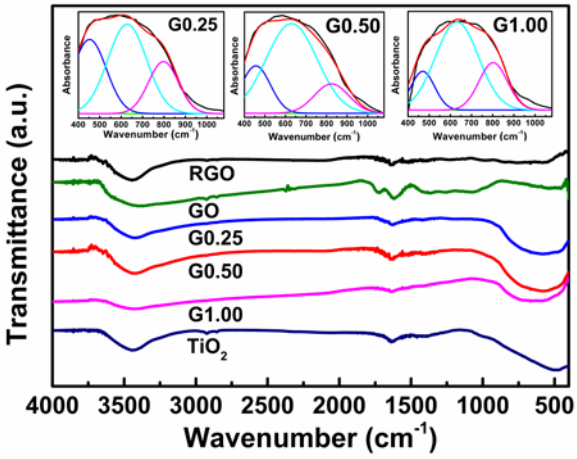

Figure 2. FTIR spectra of TiO_2, GO, RGO, G0.25, G0.50 and G1.00. Shown in the

inset is the result of deconvoluting the spectra of G0.25, G0.50 and G1.00.

3.3 XPS spectra analysis

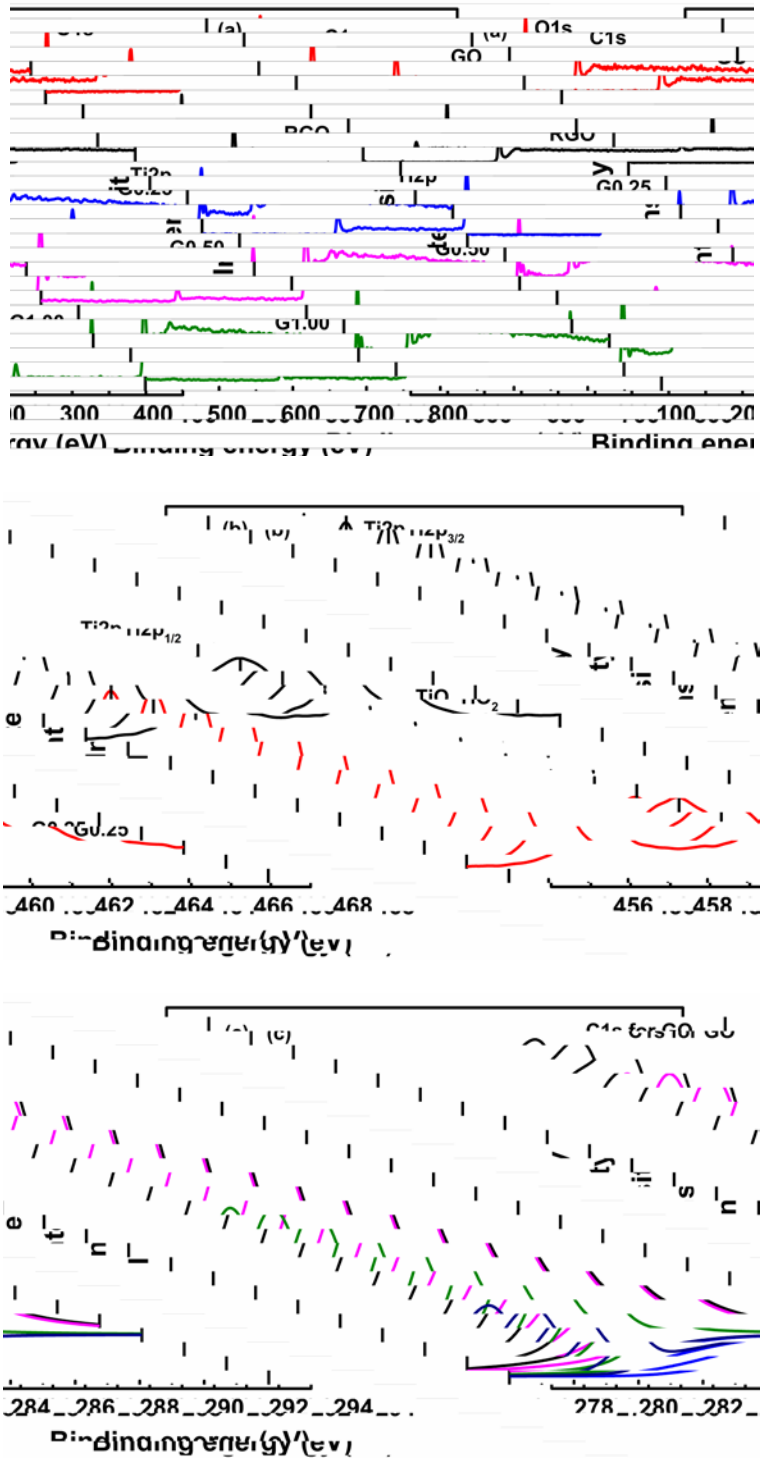

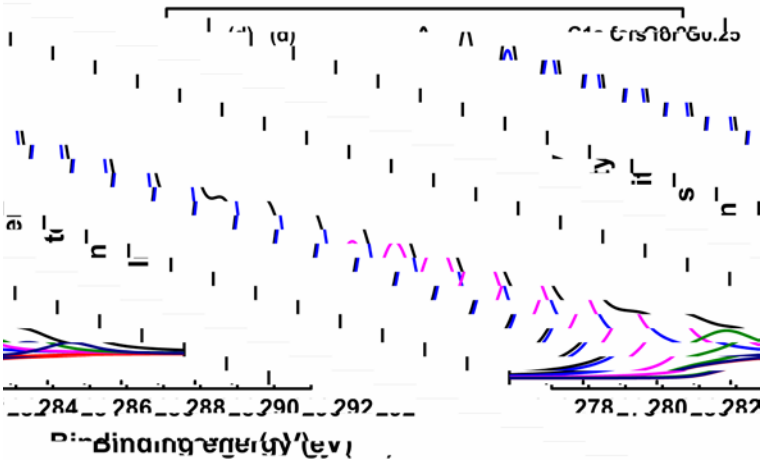

Figure 3. (a) XPS survey spectra of GO, RGO, G0.25, G0.50 and G1.00; (b) Ti 2p core level XPS spectra of TiO_2 and G0.25; High-resolution XPS spectra of C 1s for (c) GO and (d) the G0.25 nanocomposite.

The TiO_2/RGO nanocomposites were characterized by XPS. From Figure 3(a), it can be seen that after thermal reduction, RGO shows a very weak O 1s signal which is much smaller than that of GO. This implies that a trace of residual oxygen functionalities still exists in the structure of RGO. For the TiO_2/RGO nanocomposites, a new peak corresponding to Ti 2p can be clearly identified, with the binding energies at approximately 458.00, 459.00 and 457.00 eV for G0.25, G0.50 and G1.00, respectively. Figure 3(b) displays the Ti core XPS spectra of as-synthesized TiO_2 and the G0.25 nanocomposite. The Ti core-level XPS spectrum of TiO_2 exhibits two peaks centered at 464.25 and 458.50 eV, corresponding respectively to the Ti $2p_{1/2}$ and Ti $2p_{3/2}$ photoelectrons in the Ti^{4+} state [34]. For the G0.25 nanocomposite, these two peaks occur at 464.58 and 458.83 eV, respectively. In each sample, the splitting between the two Ti-bands is about 5.75 eV, consistent with the presence of Ti^{4+} in the TiO_2 and G0.25 nanocomposite [35]. The difference between the positions of the Ti peak of pure TiO_2 and that of the G0.25 nanocomposite may be assigned to the interactions of Ti with the oxygen centers of RGO. To investigate the carbon states in the nanocomposites, the high-resolution C 1s core levels of GO and G0.25 have been measured, as shown in Figures 3(c) and 3(d). Three typical peaks of GO observed at 283.90, 285.10 and 287.00 eV are usually ascribed to C=C and C-C bonds from GO,

and the oxygen-containing carbonaceous bands, respectively [6]. For the G0.25 nanocomposite, the asymmetrical and broad features of the observed C 1s XPS spectrum indicates the co-existence of distinguishable models. Deconvolution of the C 1s peaks shows the presence of chemically different C species in the TiO_2 matrix, with their binding energies at approximately 283.80, 285.20, 287.00, and 288.70 eV. The main C 1s peak located at 283.80 eV is attributed to defect-containing sp^2-hybridized carbons. The sharp peak located at 285.20 eV is assigned to the presence of C-C bonds in RGO. In addition, there is a relatively weak peak located at 288.70 eV, contributed by carboxyl carbon (O=C-O) [36]. Such a surface functional group suggests that the –OH groups on the TiO_2 nanoparticles may react with the –COOH groups on the GO surface through esterification to form O=C-O-Ti bonds [37-39]. Moreover, the intensity of the peak at around 287.0 eV for the oxygen-containing groups decreases markedly and a notable enhancement of the sp^2-C signal intensity corresponding to the C=C bond was observed in the C 1s XPS on proceeding to the G0.25 nanocomposite, implying that the introduced GO has been efficiently converted to RGO by thermal reduction. The peak ascribed to Ti-C bonds at around 282.00 eV is not detected in the G0.25 nanocomposite, indicating that carbon was not doped into the lattice of TiO_2 due to the low synthesis temperature. Similar results are also observed for G0.50 and G1.00 as are seen with G0.25, the results being shown in Figure S3.

3.4 UV-Vis spectra analysis

The UV-Vis diffuse reflectance spectra of the G0.25, G0.50 and G1.00 samples were carried out at room temperature; for comparison, the optical properties of TiO_2 nanoparticles were also measured under the same conditions. As shown in Figure 4(a), all samples exhibit some absorption in the visible region, with a λ_{onset} at 380-400 nm. The absorption of TiO_2 at ca. 400 nm is ascribed to charge transfer from the valence band (mainly formed from 2p orbitals of the oxide anions) to the conduction band (mainly formed from 3d t_{2g} orbitals of the Ti^{4+} cations) [40]. The presence of the varying amounts of TiO_2 significantly affects the light absorption of the TiO_2/RGO nanocomposites; light absorption intensity in the UV region is significantly decreased

upon doping for all of the TiO_2/RGO nanocomposites with different addition ratios of TiO_2. Fan et al. [41] and Kim et al. [42] both observed a red-shift of the absorption edge of TiO_2 and consequently a narrowing of the band gap of TiO_2 upon doping with RGO. In the present study, a red-shift to longer wavelength of the absorption edge of the TiO_2/RGO nanocomposites has also been observed, indicating a narrowing of the band gap of TiO_2 which should improve charge transfer from the valence band to the conduction band. The red shift has been assigned to the formation of Ti-O-C bonds and the direct interaction between TiO_2 and RGO [29,30,32,34,41-44], similar to that observed for carbon-doped TiO_2 nanoparticles [40], and consistent with the results from FTIR spectroscopy and XPS analysis. The maximum red-shift is observed for the G1.00 sample, which also has an absorption tail spanning the visible spectrum because of the formation of nanocomposites.

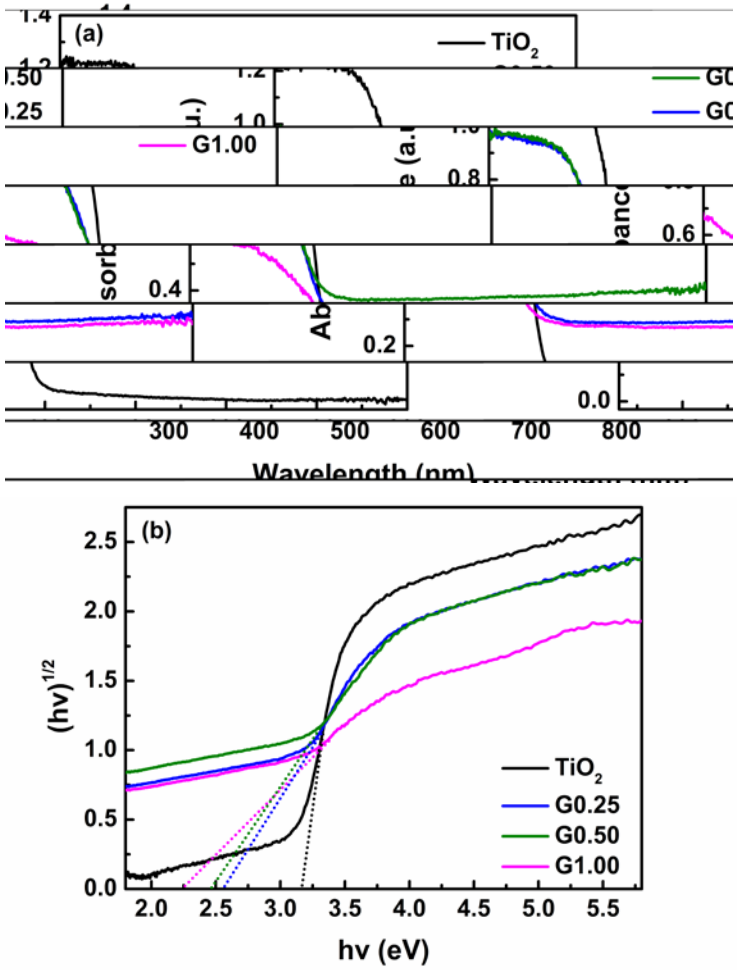

Figure 4. (a) UV-Vis diffuse reflectance spectra of the TiO_2, G0.25, G0.50 and G1.00 samples; (b) Tauc plots of the transformed Kubelka-Munk function versus the energy

of light.

The indirect band gap, E_g, of TiO_2/RGO nanocomposites near the absorption edge can be obtained from the plot of the modified Kubelka-Munk function, i.e. $(\alpha hv)^{1/2}$, versus the energy of exciting light (hv). The absorption coefficient α is related to E_g by:

$$\alpha hv = A(hv-E_g)^{1/2}$$

where hv is the incident photon energy and A is a constant for indirect transition [44]. Figure 4(b) displays the intercepts of tangents to the $(\alpha hv)^{1/2}$ versus photon energy (hv) plots, from which the (approximate) band gaps 2.26, 2.46, 2.57 and 3.16 eV for G1.00, G0.50, G0.25 and TiO_2, respectively, can be obtained. This indicates that the interaction between TiO_2 and RGO increases with the increase in TiO_2 content, and further supports the qualitative observation of a red-shift in the absorption edge of TiO_2/RGO nanocomposites compared with the pure TiO_2. The measured energy gap of 3.16 eV for TiO_2 is consistent with the anatase crystalline state. Similar results were also observed for carbon nanotubes/TiO_2 composites due to chemical bonding between the specific carbon sites and TiO_2 [45]. The maximum band-gap narrowing (0.9 eV) is comparable with the value of 0.14 eV observed for carbon-modified TiO_2 [40].

3.5 Photoluminescence spectra analysis

For nanostructured materials, photoluminescence spectra are a useful probe of the transfer efficiency of the photoinduced electrons and holes, because the photoluminescence emission comes from recombination of the free charge carriers [46]. Figures S4 and 5 display the excitation and emission photoluminescence spectra of pure TiO_2 and the TiO_2/RGO composites (G0.25, G0.50 and G1.00). The three TiO_2/RGO composites exhibit an excitation spectrum centered at *ca.* 348 nm, behavior consistent with that of pure TiO_2 (Figure S4). Upon excitation at 348 nm, the photoluminescence spectra of the TiO_2/RGO composites are similar to that of pure TiO_2 but with different intensity (Figure 5). It is well known that photoluminescence emission is the result of recombination of the excited holes and electrons either indirectly (via a band-gap state) or directly (band-band), so a higher

photoluminescence intensity may indicate a higher recombination rate of electrons and holes [47,48]. There is a decrease in photoluminescence intensity in proceeding from pure TiO_2 to the composite samples. This can be attributed to the electrons being excited from the valence band to the conduction band and then transferred to the RGO sheets because of the abundant electron-accepting sites of the latter, hindering electron-hole pair recombination. It can therefore be concluded that the presence of RGO in the nanocomposite samples might be effective in enhancing the separation efficiency of electron-hole pairs. If this is the case, then this photoluminescence quenching may afford a measure of the interfacial charge transfer via the Ti-O-C linkages and consequent electronic interactions between the RGO and TiO_2 nanoparticles in the TiO_2/RGO nanocomposites [6]. The photoluminescence of these samples was also investigated with an excitation wavelength of 300 nm (Figure S5). Consistent with the aforementioned results, a significant fluorescence quenching was observed for the TiO_2/RGO nanocomposites, providing further evidence for significant electronic communication between TiO_2 and RGO in the excited state.

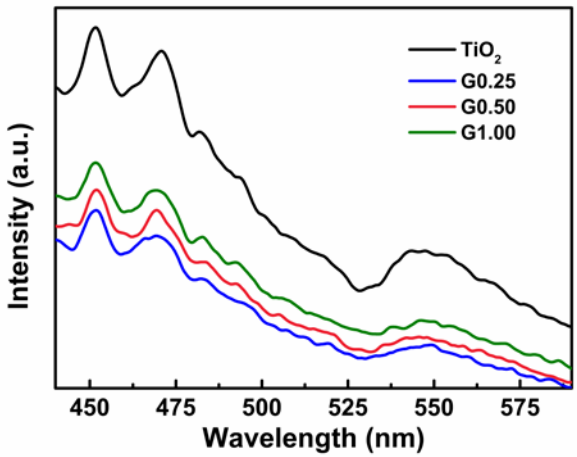

Figure 5. Emission photoluminescence spectra of the TiO_2, G0.25, G0.50 and G1.00 samples.

3.6 Raman spectra analysis

Raman spectroscopy was used to characterize the TiO_2/RGO nanocomposites as well as the as-prepared RGO. RGO exhibits a prominent D-band at 1345 cm^{-1},

corresponding to the breathing mode of κ-point phonons of A_{1g} symmetry. There is also an intense tangential mode at 1580 cm^{-1} (the G-band), which arises from the first-order scattering of E_{2g} phonons from sp^2 carbon atoms [18], as shown in the inset of Figure 6. For the TiO_2/RGO composites, several characteristic bands were observed at ca. 152, 399, 513, and 636 cm^{-1}, corresponding to the $E_{g(1)}$, $B_{1g(1)}$, A_{1g} + $B_{1g(2)}$, and $E_{g(2)}$ modes of anatase, respectively [49]. Generally, the full-width at half-maximum (FWHM) of the anatase E_g mode increases with decreasing crystallite size of anatase [50]; in the present case, the peak intensities of the E_g mode are significantly increased and the peak widths are broadened on increasing addition of TiO_2, consistent with decreasing particle size. Significantly, D- and G-bands for graphitized structures were also observed, confirming the presence of RGO in the TiO_2/RGO composites. The frequencies of these spectral features match those of pristine graphite, consistent with the reduction of GO. The intensity ratio of the D/G bands provides a measure of the disorder/defects in RGO, a smaller intensity ratio of I_D/I_G corresponding to larger average size and fewer sp^3 defects/disorders of the in-plane graphitic crystallite sp^2 domains. In the present case, the intensity ratio of I_D/I_G for RGO is 0.94, increasing to 1.06, 1.03 and 1.05 for G0.25, G0.50 and G1.00, respectively. This is consistent with the newly formed graphitic domains being smaller in size and greater in number than those in GO before the hydrothermal treatment, as reported by Shah and coworkers [51]. The plane crystallite size, L_a, characterizing the RGO domains can be obtained from the equation:

$$L_a(nm) = \frac{560}{E_\lambda^4}\left(\frac{I_D}{I_G}\right)^{-1}$$

where E_λ is the excitation energy in eV [1]. Thus, RGO has an L_a of ~20.2 nm, which upon functionalization reduces to ~17.9, ~18.4 and ~18.1 nm for G0.25, G0.50 and G1.00, respectively. This change further confirms a decrease in the average size and a higher defect density of the in-plane graphitic crystallite sp^2 domains upon reduction of the exfoliated GO, suggesting a decrease in the oxygen-containing groups on RGO, and consistent with the results of FTIR.

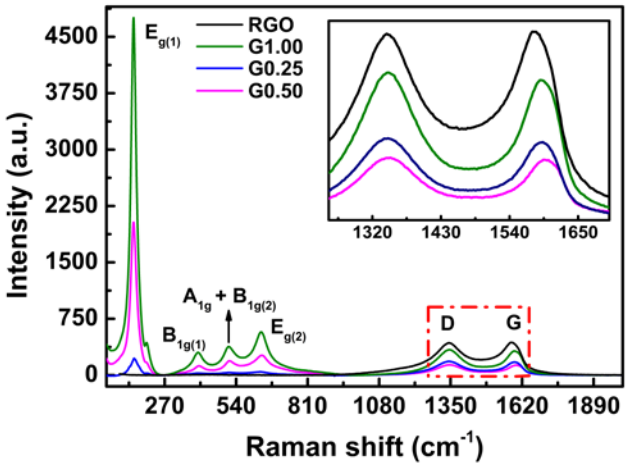

Figure 6. Raman spectra of the RGO, G0.25, G0.50 and G1.00 samples.

3.7 XRD studies

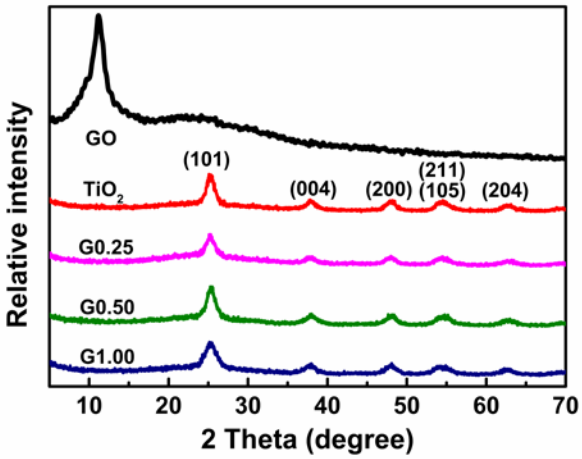

Figure 7. XRD patterns of the GO, TiO_2, G0.25, G0.50 and G1.00 samples.

Figure 7 displays the XRD patterns of the TiO_2, G0.25, G0.50 and G1.00 samples, together with the pattern of GO. In the case of GO, the peak at 11.2° indicates a large interlayer distance of 0.78 nm that results from the presence of oxygenated functional groups on the graphene sheets. The reflections in the XRD patterns of TiO_2 and the TiO_2/RGO composites can be indexed to anatase TiO_2 (JCPDS Card No. 21-1272) [37,52,53]; no rutile phase TiO_2 was detected in this work. The typical diffraction peaks of RGO were not found in the XRD patterns of the nanocomposites, a result

that may derive from the main peak of anatase TiO_2 masking the main characteristic peak of RGO [24]. The same phenomenon was observed in a previous paper [53], indicating that GO was reduced to RGO during the hydrothermal process, and consistent with the results from XPS. Similar XRD patterns of anatase TiO_2 nanoparticles from different samples indicate that the incorporation of RGO has little influence on the phase structure of TiO_2 during the hydrothermal process.

3.8 TEM studies

Typical TEM images of the RGO and TiO_2/RGO composites are shown in Figure 8. Samples for TEM analysis were obtained by spreading a drop of a dilute dispersion of the as-prepared products on amorphous carbon-coated copper grids that were then dried in air before transfer to the TEM sample chamber. Figure 8(a) reveals that, as expected, the RGO starting material is composed of single- and multi-layer RGO sheets; a large single-layer RGO flake is visible, as well as a large number of multi-layer RGO sheets. The flakes are almost transparent and entangled with each other, resembling a crumpled silk veil [54]; it is impossible to determine the number of layers. The TEM images of the TiO_2/RGO nanocomposites reveal that the composites are composed of RGO sheets and many small TiO_2 nanoparticles. Since the monolayer RGO sheets are extremely thin, it was difficult to distinguish between them and the carbon-supported films on the copper grid. Nevertheless, the edges and crumpled silk waves of these RGO nanosheets confirm that the TiO_2 nanoparticles are indeed deposited on the supports (the almost transparent RGO sheets). During formation of the composites, the TiO_2 nanoparticles adhere to the functional groups on the GO plane, with simultaneous reduction of GO to RGO by electron donation from ethanol and formation of Ti-O-C bonding between TiO_2 and RGO [55]. A majority of the TiO_2 nanoparticles are anchored to the RGO sheets (there is a very small amount of free-standing TiO_2 particles), which is very important as it ensures efficient electron collection via the RGO sheets during the insertion/extraction processes. Our TEM measurements further reveal that the increase in tetrabutyl titanate content in the hydrothermal process increases the dispersion of the TiO_2 nanoparticles on the RGO sheets.

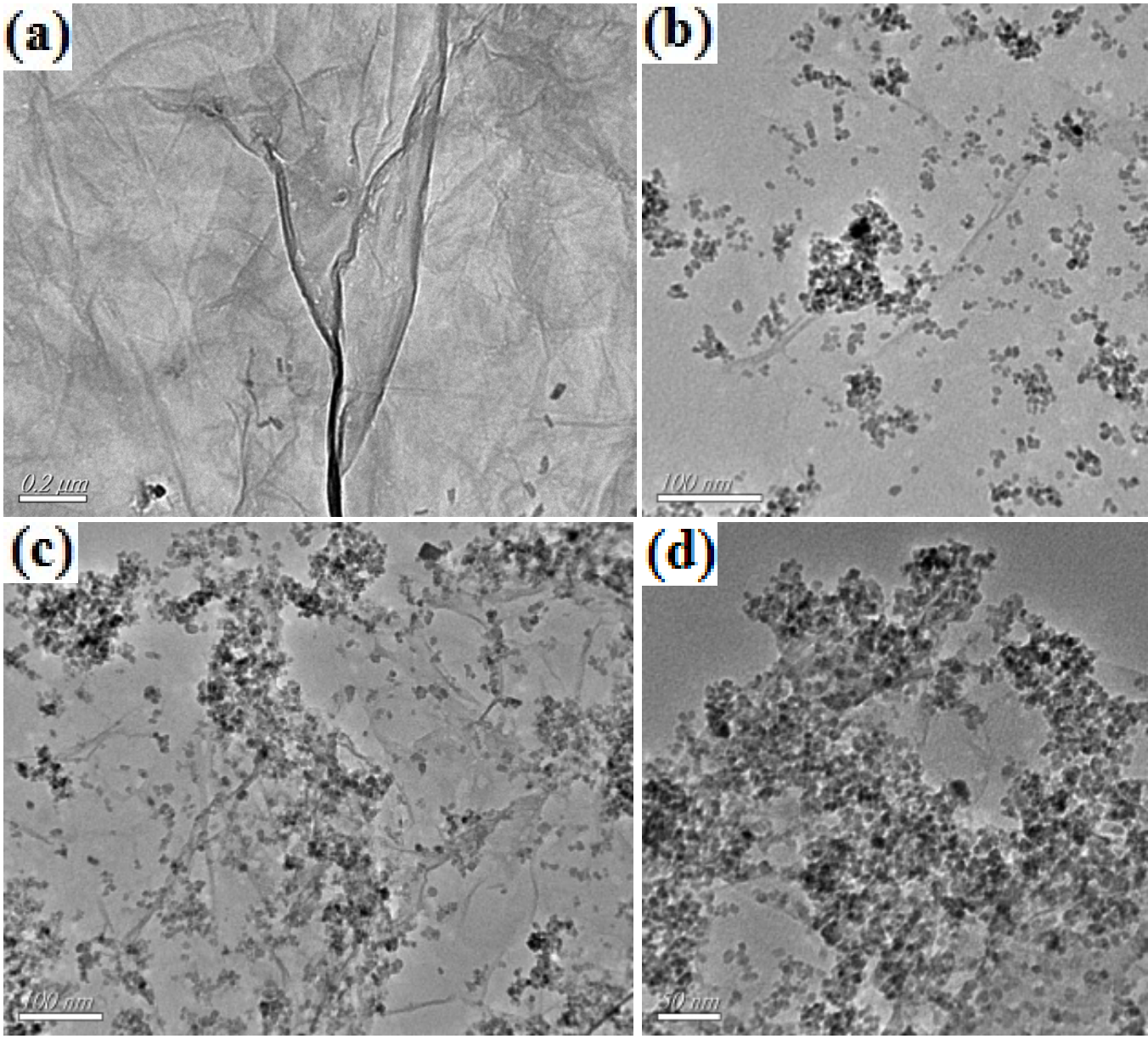

Figure 8. TEM spectra of the RGO (a), G0.25 (b), G0.50 (c) and G1.00 (d) samples.

3.9 Nonlinear absorption and optical limiting behaviour

Recent process in the field of photonics and optoelectronics has encouraged the search for materials with excellent NLO properties and ultrafast response, with the goal of protecting sensitive optical systems and human eyes [56]. Various materials such as organic molecules [57], inorganic complexes [58], organometallic compounds [59], nanocomposites, and semiconductors [60] have been intensively studied (both theoretically and experimentally) for potential applications in OL. Among the various possible NLO materials, nanocomposites have proven to be superior candidates

because of their outstanding mechanical, electrical and thermal properties [1,61]. Nanocomposites can exhibit strong nonlinear extinction (including, inter alia, absorption, scattering and/or refraction) for intense laser beams and thus may be viable OL materials [62]. Successful implementation of their exceptional performance is still lacking due to the limited knowledge of the microstructures of nanomaterials, information on which is needed to design and control their physicochemical properties and to clarify their NLO mechanisms. Recently, the NLO properties of TiO_2 in nanoscale composite materials has received considerable interest (for example, large reverse-saturable absorption resulting from an accumulative effect of two-photon absorption and electric charge interaction was observed in poly(methyl methacrylate)/TiO_2 nanocomposites [63]), while zinc oxide-decorated RGO sheets have been shown to exhibit excellent nonlinear properties compared to the individual components [6]. However, NLO studies of metal decorated RGO, especially metal oxide-decorated RGO, are still scarce, so the OL properties of the nanocomposites prepared in the present studies have been assessed.

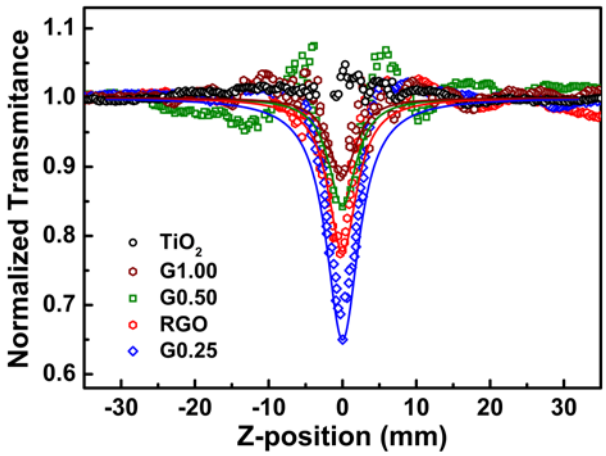

Figure 9. Normalized transmittance curves of pure TiO_2, RGO, G0.25, G0.50 and G1.00. Solid curves represent the theoretical fits to the experimental data.

Figure 9 displays representative open-aperture Z-scan curves of pure TiO_2, RGO and TiO_2-doped RGO nanocomposites as solutions in DMF. For ease of comparison, the concentrations of all samples were adjusted to the same linear transmittance (60%

at 532 nm). As shown in Figure 9, solutions of G0.25, G1.00 and RGO exhibit decreased normalized transmittance with valley-shaped curves as they are brought to the beam waist, consistent with a strong reverse saturable absorption (RSA) response with 4 ns pulse excitation, and OL behavior. For an optical limiter, the depth of the valley in the open-aperture Z-scan curves is correlated with the OL merit [64]. The largest decrease in transmittance value is observed for the G0.25 nanocomposite, suggesting that it should have the best OL performance. Because the solvent DMF exhibits no nonlinear absorption under these experimental conditions, the observed nonlinear absorption must arise from the solutes. The nonlinearity of pure TiO_2 was also investigated under the same experimental conditions, but no obvious signal was observed, suggesting that the TiO_2 has a very small NLO effect that can be neglected. For a quantitative comparison, we have carried out a theoretical fitting of the experimental results to obtain effective nonlinear absorption coefficients β_{eff} (m/W). With the same linear transmittance, the G0.25 nanocomposite exhibits a better NLO effect, with a nonlinear absorption coefficient β_{eff} of 6.0×10^{-10} m/W, compared to those of RGO (3.0×10^{-10} m/W), G1.00 (1.3×10^{-10} m/W) and G0.50 (1.9×10^{-10} m/W), indicating a significant influence of the TiO_2 concentration in the nanocomposites on the NLO response. Similar phenomena have been observed with multiwalled carbon nanotube-organically modified silicate nanohybrid gel glass (MWCNT-ORMOSIL) [65]. Comparing the values of β_{eff} for the G0.25 nanocomposite obtained in the present work with that reported previously for the MWCNT-ORMOSIL system in Ref. [65] reveals that G0.25 has a larger effective nonlinear absorption coefficient, though the differing experimental geometries render such a comparison necessarily cautious.

Interestingly, the curve for G0.50 clearly displays firstly saturable absorption (SA) and then RSA behavior, and then a return to SA behavior as the sample traverses in the *z*-direction. Slower excited-state (S_1) relaxation and faster higher-lying excited-state (S_n) relaxation play a dominant role in switching the NLO absorption performance from SA to RSA and back to SA [66]. The S_1 state is populated by relaxation from the higher excited state and from ground-state absorption. The S_n state

is populated by ESA corresponding to the S_1-S_n transition [67]. The lifetime of the S_1 state is longer, and thus G0.50 is readily saturated in the (relatively) low-intensity region. At higher intensities, two-photon absorption (TPA) and the formation of strong light scattering centers may dominate for G0.50, resulting in a RSA effect [68]. Taken together, the observed Z-scan profile is consistent with a combination of ESA (the S_1-S_n transition), light scattering and a TPA process. Pure RGO displays a clear-cut RSA behavior resulting from a TPA process. The present study reveals that there is an optimum concentration of TiO_2 in the nanocomposites for NLO behavior, specifically compositions G0.25 and G0.50, which have the strongest RSA behavior and combination of NLO mechanisms, respectively. The nonlinear absorption of nanocomposite G1.00 is the weakest, possibly due to the loading of TiO_2 being so great that it results in formation of a hydrolyzed titanium alkoxide network structure instead of individual oxide nanoparticles [63]; as a result, the quantum confinement effect responsible for NLO performance decreases significantly. The magnitude of the nonlinear absorption observed for the three nanocomposites is relatively small compared to previously-reported porphyrin-graphene or phthalocyanine-graphene nanocomposites [69-71]. However, the different NLO response obtained with these nanocomposites suggests that TiO_2 doped-RGO holds promise for various potential applications. For example, the significant NLO performance of the G0.25 nanocomposite may lead to OL applications in eye and sensor protection, while the NLO mechanism changing from SA to RSA and back to SA as a function of light intensity for G0.50 indicates that it can be a potential candidate for ultrafast NLO switching applications.

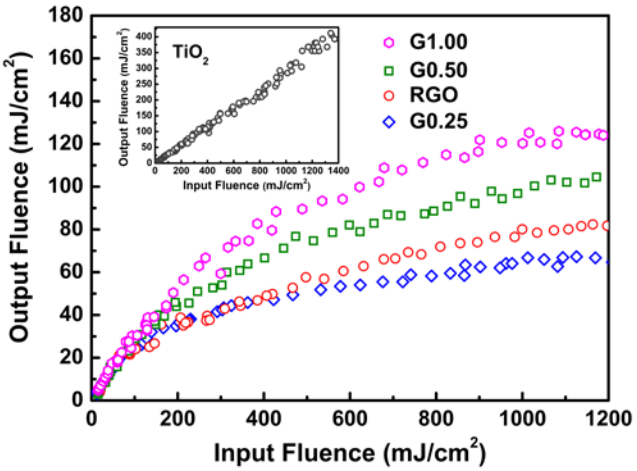

Figure 10. Comparison of the optical limiting performance of RGO, G0.25, G0.50 and G1.00 in DMF at 532 nm. Shown in the inset is the optical limiting response of TiO_2.

RGO, G0.25, G0.50 and G1.00 exhibit nonlinear absorption, so these materials can in principle function as optical limiters to nanosecond 532 nm laser pulses (Figure 10). For comparison, the OL performance of TiO_2 was investigated, but no obvious limiting response was observed, consistent with the result from open-aperture Z-scan (Figure 9). From Figure 10, it can be clearly seen that, at low input fluences, dispersions of these species (RGO, G0.25, G0.50 and G1.00) obey Beer's Law (linear relationships between input fluence and output fluence). As the incident fluence increases, the output fluence deviates from linearity, consistent with an OL response. Experiments with pure DMF solvent exhibited no detectable OL response under the same conditions, implying that the solvent contribution is negligible; the observed OL effect should thus be assigned solely to the solutes. Compared to the RGO, G0.50 and G1.00 dispersions, the G0.25 nanocomposite displays an enhanced OL response, consistent with the results of open-aperture Z-scan, and presumably due to a combination of the NLO mechanisms of RGO and TiO_2 in the nanocomposite G0.25; RGO exhibits large ESA and TPA in the nanosecond regime, resulting in enhanced nonlinear absorption performance in RGO-containing composites [72]. As shown in Figure 9, G0.25 has the largest dip among the normalized transmittance curves, and thus G0.25 exhibits a much better OL response than RGO, G0.50 or G1.00. The

enhanced OL in G0.25 may have a significant contribution from defect-induced states that are generated during preparation, and which facilitate interband transitions through ESA [1,73]; the increase in the number of defects is confirmed by the increased I_D/I_G ratio after heat-treatment (Figure 6). Significant fluorescence quenching of TiO_2 following doping with RGO is observed, due to the electron/energy transfer from TiO_2 to RGO. This doping may inhibit the recombination of electron-hole pairs, and thus accelerate the transfer of photogenerated electrons. During the synthesis of the G0.25 nanocomposite, some oxygen-containing groups on the surface of GO are partially removed by hydrothermal treatment, and the extended conjugation is thereby further increased. The larger the extent of conjugation, the higher the chance for electron/energy transfer, leading to enhanced OL response [6].

4. Conclusion

In summary, we have reported the hydrothermal synthesis and structural, spectroscopic and NLO properties of TiO_2/RGO nanocomposites. The formation of the nanocomposites was confirmed by FTIR, XPS, optical absorption, XRD and Raman spectroscopies, and TEM micrographs. Compared to TiO_2, significant fluorescence quenching was observed for all nanocomposites, suggesting energy transfer. The NLO absorption properties and optical limiting responses of the nanocomposites were investigated using the Z-scan technique at 532 nm with 4 ns laser pulses. The present study suggests that there is an optimum concentration of TiO_2 in the nanocomposites to maximize NLO behavior; the G0.25 nanocomposite exhibits enhanced NLO performance in the nanosecond regime, ascribed to a combination of NLO mechanisms, while intensity-dependent behavior in G0.50 is observed because of the combined contribution of ESA and TPA. Overall, these results suggest that TiO_2/RGO nanocomposites with an appropriate content of TiO_2 afford good candidates for optical limiting and NLO switching, and potentially attractive possibilities for ultrafast nonlinear optical materials for photonic and optoelectronic devices.

Acknowledgements

Financial support from the National Natural Science Foundation of China (51432006, 50925207, 51172100), the Ministry of Science and Technology of China for the International Science Linkages Program (2009DFA50620, 2011DFG52970), the Ministry of Education of China for the Changjiang Innovation Research Team (IRT1064), the Ministry of Education and the State Administration of Foreign Experts Affairs for the 111 Project (B13025), and Jiangsu Innovation Research Team are gratefully acknowledged. M.G.H. and M.P.C. thank the Australian Research Council for support.

References

[1] Anand B, Kaniyoor A, Sai SS, Philip R, Ramaprabhu S. Enhanced optical limiting in functionalized hydrogen exfoliated graphene and its metal hybrids. J Mater Chem C 2013;1:2773-80.

[2] Yang SB, Wu XL, Chen CG, Dong HL, Hu WP, Wang XK. Spherical α-Ni(OH)$_2$ nanoarchitecture grown on graphene as advanced electrochemical pseudocapacitor materials. Chem Commun 2012;48:2773-5.

[3] Allen MJ, Tung VC, Kaner RB. Honeycomb carbon: a review of graphene. Chem Rev 2010;110:132-45.

[4] Xue YZ, Wu B, Jiang L, Guo YL, Huang LP, Chen JY, et al. Low temperature growth of highly nitrogen-doped single crystal graphene arrays by chemical vapor deposition. J Am Chem Soc 2012;134:11060-3.

[5] Compton OC, Nguyen ST. Graphene oxide, highly reduced graphene oxide, and graphene: Versatile building blocks for carbon-based materials. Small 2010;6:711-23.

[6] Zhang B, Liu G, Chen Y, Zeng LJ, Zhu CX, Neoh KG, et al. Conjugated polymer-grafted reduced graphene oxide for nonvolatile rewritable memory. Chem Eur J 2011;17:13646-52.

[7] Bonaccorso F, Sun Z, Hasan T, Ferrari AC. Graphene photonics and optoelectronics. Nat Photonics 2010;4:611-22.

[8] Eisenthal KB. Second harmonic spectroscopy of aqueous nano- and microparticle interfaces. Chem Rev 2006;106:1462-77.

[9] Chan SC, Barteau MA. Preparation of highly uniform Ag/TiO$_2$ and Au/TiO$_2$ supported nanoparticle catalysts by photodeposition. Langmuir 2005;21:5588-95.

[10] Ravirajan P, Haque SA, Durrant JR, Bradley DDC, Nelson J. The effect of polymer optoelectronic properties on the performance of multilayer hybrid polymer/TiO$_2$ solar cells. Adv Funct Mater 2005;15:609-18.

[11] Zhang L, Cole JM, Dai CC. Variation in optoelectronic properties of azo dye-sensitized TiO$_2$ semiconductor interfaces with different adsorption anchors: Carboxylate, sulfonate, hydroxyl and pyridyl groups. ACS Appl Mater Interfaces

2014;6:7535-46.

[12] Wang JTW, Ball JM, Barea EM, Abate A, Alexander-Webber JA, Huang J, et al. Low-temperature processed electron collection layers of graphene/TiO_2 nanocomposites in thin film perovskite solar cells. Nano Lett 2014;14:724-30.

[13] George S, Pokhrel S, Ji ZX, Henderson BL, Xia T, Li LJ, et al. Role of Fe doping in tuning the band gap of TiO_2 for the photo-oxidation-induced cytotoxicity paradigm. J Am Chem Soc 2011;133:11270-8.

[14] Chen WC, Lee SJ, Lee LH, Lin JL. Synthesis and characterization of trialkoxysilane-capped poly(methyl methacrylate)-titania hybrid optical thin films. J Mater Chem 1999;9:2999-3003.

[15] Lee LH, Chen WC. High-refractive-index thin films prepared from trialkoxysilane-capped poly(methyl methacrylate)-titania materials. Chem Mater 2001;13:1137-42.

[16] Yuwono AH, Liu BH, Xue JM, Wang J, Elim HI, Ji W, et al. Controlling the crystallinity and nonlinear optical properties of transparent TiO_2-PMMA nanohybrids. J Mater Chem 2004;14:2978-87.

[17] Liu JC, Bai HW, Wang YJ, Liu ZY, Zhang XW, Sun DD. Self-assembling TiO_2 nanorods on large graphene oxide sheets at a two-phase interface and their anti-recombination in photocatalytic applications. Adv Funct Mater 2010;20:4175-81.

[18] Zhang D, Xie FX, Lin P, Choy CH. Al-TiO_2 composites-modified single-layer graphene as an efficient transparent cathode for organic solar cells. ACS Nano 2013;7:1740-7.

[19] Ellmer K. Past achievements and future challenges in the development of optically transparent electrodes. Nat Photonics 2012;6:809-17.

[20] Wang AJ, Long LL, Zhao W, Song YL, Humphrey MG, Cifuentes MP, et al. Increased optical nonlinearities of graphene nanohybrids covalently functionalized by axially-coordinated porphyrins. Carbon 2013;53:327-38.

[21] Wang AJ, Long LL, Meng SC, Li XF, Zhao W, Song YL, et al. Cooperative enhancement of optical nonlinearities in a porphyrin derivative bearing a

pyrimidine chromophore at the periphery. Org Biomol Chem 2013;11:4250-7.

[22] Hummers WS, Offeman R.E. Preparation of graphitic oxide. J Am Chem Soc 1958;80:1339.

[23] Nethravathi C, Rajamathi M. Chemically modified graphene sheets produced by the solvothermal reduction of colloidal dispersions of graphite oxide. Carbon 2008;46:1994-8.

[24] Zhang YH, Tang ZR, Fu XZ, Xu YJ. TiO_2-graphene nanocomposites for gas-phase photocatalytic degradation of volatile aromatic pollutant: Is TiO_2-graphene truly different from other TiO_2-carbon composite materials? ACS Nano 2010;4:7303-14.

[25] Liang YY, Wang HL, Casalongue HS, Chen Z, Dai HJ. TiO_2 nanocrystal grown on graphene as advanced photocatalytic hybrid materials. Nano Res 2010;3:701-5.

[26] Han JT, Kim BJ, Kim BG, Kim JS, Jeong BH, Jeong SY, et al. Enhanced electrical properties of reduced graphene oxide multilayer films by in-situ insertion of a TiO_2 layer. ACS Nano 2011;5:8884-91.

[27] Shen JF, Shi M, Yan B, Ma HW, Li N, Ye MX. Ionic liquid-assisted one-step hydrothermal synthesis of TiO_2-reduced graphene oxide composites. Nano Res 2011;4:795-806.

[28] Park S, Lee KS, Bozoklu G, Cai W, Nguyen ST, Ruoff RS. Graphene oxide papers modified by divalent ions-enhancing mechanical properties via chemical crossing-linking. ACS Nano 2008;2:572-8.

[29] Liang DY, Cui C, Hu HH, Wang YP, Xu S, Ying BL, et al. One-step hydrothermal synthesis of anatase TiO_2/reduced graphene oxide nanocomposites with enhanced photocatalytic activity. J Alloys Comp 2014;582:236-40.

[30] Zhang H, Lv XJ, Li YM, Wang Y, Li JH. P25-Graphene composite as a high performance photocatalyst. ACS Nano 2009;4:380-6.

[31] Gao YY, Pu XP, Zhang DF, Ding GQ, Shao X, Ma J. Combustion synthesis of graphene oxide-TiO_2 hybrid materials for photodegradation of methyl orange. Carbon 2012;50:4093-101.

[32] Wu HT, Fan J, Liu EZ, Hu XY, Ma YN, Fan X, et al. Facile hydrothermal synthesis of TiO_2 nanospindles-reduced graphene oxide composite with a enhanced photocatalytic activity. J Alloys Comp 2015;623:298-303.

[33] Sakthivel S, Shankar MV, Palanichamy M, Arabindoo B, Bahnemann DW, Murugesan V. Enhancement of photocatalytic activity by metal deposition: characterisation and photonic efficiency of Pt, Au and Pd deposited on TiO_2 catalyst. Water Res 2004;38:3001-8.

[34] Selim M, Shah AS, Park AR, Zhang K, Park JH, Yoo PJ. Green synthesis of biphasic TiO_2-reduced graphene oxide nanocomposites with highly enhanced photocatalytic activity. ACS Appl Mater Interfaces 2012;4:3893-901.

[35] Jiang GD, Lin ZF, Chen C, Zhu LH, Chang Q, Wang N, et al. TiO_2 nanoparticles assembled on graphene oxide nanosheets with photocatalytic activity for removal of pollutants. Carbon 2011;49:2693-701.

[36] Akhavan O, Ghaderi E. Photocatalytic reduction of graphene oxide nanosheets on TiO_2 thin film for photoinactivation of bacteria in solar light irradiation. J Phys Chem C 2009;113:20214-20.

[37] Xiang QJ, Yu JQ, Jaroniec M. Enhanced photocatalytic H_2-production activity of graphene-modified titania nanosheets. Nanoscale 2011;3:3670-8.

[38] Wei W, Yu C, Zhao QF, Li GS, Wan Y. Improvement of the visible-light photocatalytic performance of TiO_2 by carbon mesostructures. Chem Eur J 2013;19:566-77.

[39] Ren WJ, Ai ZH, Jia FL, Zhang LZ, Fan XX, Zou ZG. Low temperature preparation and visible light photocatalytic activity of mesoporous carbon-doped crystalline TiO_2. Appl Catal B: Environ 2007;69:138-44.

[40] Sakthivel S, Kisch H. Daylight photocatalysis by carbon-modified titanium dioxide. Angew Chem Int Ed 2003;42:4908-11.

[41] Fan WQ, Lai QH, Zhang QH, Wang Y. Nanocomposites of TiO_2 and reduced graphene oxide as efficient photocatalysts for hydrogen evolution. J Phys Chem C 2011;115:10694-701.

[42] Kim YK, Min DH. UV protection of reduced graphene oxide films by TiO_2

nanoparticle incorporation. Nanoscale 2013;5:3638-42.

[43] Lee JS, You KH, Park CB. Highly photoactive, low bandgap TiO_2 nanoparticles wrapped by graphene. Adv Mater 2012;24:1084-8.

[44] Sciancalepore C, Cassano T, Curri ML, Mecerreyes D, Valentini A, Agostiano A, et al. TiO_2 nanorods/PMMA copolymer-based nanocomposites: highly homogeneous linear and nonlinear optical material. Nanotechnology 2008;19:205705.

[45] Woan K, Pyrgiotakis G, Sigmund W. Photocatalytic carbon-nanotube-TiO_2 composites. Adv Mater 2009;21:2233-9.

[46] Zhou KF, Zhu YH, Yang XL, Jiang X, Li CZ. Preparation of graphene-TiO_2 composites with enhanced photocatalytic activity. New J Chem 2011;35:353-9.

[47] Yu JG, Ma TT, Liu G, Cheng B. Enhanced photocatalytic activity of bimodal mesoporous titania powders by C_{60} modification. Dalton Trans 2011;40:6635-44.

[48] Lin C, Song Y, Cao LX, Chen SW. Effective photocatalysis of functional nanocomposites based on carbon and TiO_2 nanoparticles. Nanoscale 2013;5:4986-92.

[49] Xiang QJ, Yu JG, Jaroniec M. Synergetic effect of MoS_2 and graphene as cocatalysts for enhanced photocatalytic H_2 production activity of TiO_2 nanoparticles. J Am Chem Soc 2012;134:6575-8.

[50] Fresno F, Tudela D, Coronado JM, Fernández-García M, Hunqría AB, Soria J. Influence of Sn^{4+} on the structural and electronic properties of $Ti_{1-x}Sn_xO_2$ nanoparticles used as photocatalysts. Phys Chem Chem Phys 2006;8:2421-30.

[51] Li N, Liu G, Zhen C, Li F, Zhang LL, Cheng HM. Battery performance and photocatalytic activity of mesoporous anatase TiO_2 nanospheres/graphene composites by template-free self-assembly. Adv Funct Mater 2011;21:1717-22.

[52] Shen JF, Yan B, Shi M, Ma HW, Li N, Ye MX. One step hydrothermal synthesis of TiO_2-reduced graphene oxide sheets. J Mater Chem 2011;21:3415-21.

[53] Zhang XY, Li HP, Cui XL, Lin YH. Graphene/TiO_2 nanocomposites: synthesis, characterization and application in hydrogen evolution from water photocatalytic splitting. J Mater Chem 2010;20:2801-6.

[54] Stankovich S, Piner RD, Nguyen ST, Ruoff RS. Synthesis and exfoliation of isocyanate-treated graphene oxide nanoplatelets. Carbon 2006;44:3342-7.

[55] Pan X, Zhao Y, Liu S, Korzeniewski CL, Wang S, Fan ZY. Comparing graphene-TiO_2 nanowire and graphene-TiO_2 nanoparticle composite photocatalysts. ACS Appl Mater Interfaces 2012;4:3944-50.

[56] He GS, Tan LS, Zheng Q, Prasad PN. Multi-photon absorbing materials: molecular designs, syntheses, characterizations, and applications. Chem Rev 2008;108:1245-330.

[57] Raymond JE, Bhaskar A, Goodson T, Makiuchi N, Ogawa K, Kobuke Y. Synthesis and two-photon absorption enhancement of porphyrin macrocycles. J Am Chem Soc 2008;130:17212-3.

[58] Zhang C, Matsumoto T, Samoc M, Petrie S, Meng S, Corkery TC, et al. Dodecanuclear-ellipse and decanuclear-wheel nickel(II) thiolato clusters with efficient femtosecond nonlinear absorption. Angew Chem Int Ed 2010;49:4209-12.

[59] Drouet S, Merhi A, Yao D, Cifuentes MP, Humphrey MG, Wielgus M, et al. Cubic nonlinear optical properties of new zinc tetraphenyl porphyrins peripherally functionalized with electron-rich Ru(II) alkynyl substituents. Tetrahedron 2012;68:10351-9.

[60] Szeremeta J, Nyk M, Wawrzynczyk D, Samoc M. Wavelength dependence of nonlinear optical properties of colloidal CdS quantum dots. Nanoscale 2013;5:2388-93.

[61] Ray PC. Size and shape dependent second-order nonlinear optical properties of nanomaterials and their application in biological and chemical sensing. Chem Rev 2010;110:5332-65.

[62] Balapanuru J, Yang JX, Xiao S, Bao QL, Jahan M, Polavarapu L, et al. A graphene oxide-organic dye ionic complex with DNA-sensing and optical-limiting properties. Angew Chem Int Ed 2010;49:6549-53.

[63] Yuwono AH, Xue JM, Wang J, Elim HI, Ji W, Li Y, et al. Transparent nanohybrids of nanocrystalline TiO_2 in PMMA with unique nonlinear optical

behavior. J Mater Chem 2003;13:1475-9.

[64] Cheng X, Dong NN, Li B, Zhang XY, Zhang SF, Jiao J, et al. Controllable broadband nonlinear optical response of graphene dispersions by tuning vacuum pressure. Opt Express 2013;21:16486-93.

[65] Zheng C, Feng M, Du YH, Zhan HB. Synthesis and third-order nonlinear optical properties of a multiwalled carbon nanotube-organically modified silicate nanohybrid gel glass. Carbon 2009;47:2889-97.

[66] Krishna MBM, Venkatramaiah N, Venkatesan R, Rao DN. Nonlinear optical properties of graphene (OH, Sn) porphyrin composites in picosecond regime. AIP Conf Proc 2011;1391:680-2.

[67] Gurudas U, Brooks E, Bubb DM, Heiroth S, Lippert T, Wokaun A. Saturable and reverse saturable absorption in silver nanodots at 532 nm using picosecond laser pulses. J Appl Phys 2008;104:073107/1-073107/8.

[68] West R, Wang Y, Goodson III T. Nonlinear absorption properties in novel gold nanostructured topologies. J Phys Chem B 2003;107:3419-26.

[69] Krishna MBM, Venkatramaiah N, Venkatesan R, Rao DN. Synthesis and structural, spectroscopic and nonlinear optical measurements of graphene oxide and its composites with metal and metal free porphyrins. J Mater Chem 2012;22:3059-68.

[70] Zhu JH, Li YX, Chen Y, Wang J, Zhang B, Zhang JJ, et al. Graphene oxide covalently functionalized with zinc phthalocyanine for broadband optical limiting. Carbon 2011;49:1900-5.

[71] Xu YF, Liu ZB, Zhang XL, Wang Y, Tian JG, Huang Y, et al. A graphene hybrid material covalently functionalized with porphyrin: synthesis and optical limiting property. Adv Mater 2009;21:1275-9.

[72] Liu ZB, Wang Y, Zhang XL, Xu YF, Chen YS, Tian JG. Nonlinear optical properties of graphene oxide in nanosecond and picosecond regimes. Appl Phys Lett 2009;94:021902-3.

[73] Coleman VA, Knut R, Karis O, Grennberg H, Jansson U, Quinlan R, et al. Defect formation in graphene nanosheets by acid treatment: an X-ray absorption

spectroscopy and density functional theory study. J Phys D: Appl Phys 2008;41:062001-4.

Figure captions

Figure 1. Illustration of the fabrication process of the TiO_2-decorated RGO nanocomposites.

Figure 2. FTIR spectra of TiO_2, GO, RGO, G0.25, G0.50 and G1.00. Shown in the inset is the deconvolution spectra of G0.25, G0.50 and G1.00.

Figure 3. (a) XPS survey spectra of GO, RGO, G0.25, G0.50 and G1.00; (b) Ti2p core level XPS spectra of TiO_2 and G0.25; High-resolution XPS spectra of C1s for (c) GO and (d) the G0.25 nanocomposite.

Figure 4. (a) UV-Vis diffuse reflectance spectra of the TiO_2, G0.25, G0.50 and G1.00 samples; (b) Tauc plots of the transformed Kubelka-Munk function versus the energy of light.

Figure 5. Emission photoluminescence spectra of the TiO_2, G0.25, G0.50 and G1.00 samples.

Figure 6. Raman spectra of the RGO, G0.25, G0.50 and G1.00 samples.

Figure 7. XRD patterns of the GO, TiO_2, G0.25, G0.50 and G1.00 samples.

Figure 8. TEM spectra of the RGO (a), G0.25 (b), G0.50 (c) and G1.00 (d) samples.

Figure 9. Normalized transmittance curves of pure TiO_2, RGO, G0.25, G0.50 and G1.00. Solid curves represent the theoretical fits to the experimental data.

Figure 10. Comparison of the optical limiting performance of RGO, G0.25, G0.50 and G1.00 in DMF at 532 nm. Shown in the inset is the optical limiting response of TiO_2.